A HYBRID, EXPLICIT-IMPLICIT, SECOND ORDER IN SPACE AND TIME TVD SCHEME FOR TWO-DIMENSIONAL COMPRESSIBLE FLOWS

FARHANG NOROUZI AND EVGENY TIMOFEEV

McGill University, Department of Mechanical Engineering, Montreal, QC, H3A0C3, Canada
e-mails: farhang.norouzi@mail.mcgill.ca; evgeny.timofeev@mcgill.ca

Key words: Hybrid Scheme, TVD Scheme, Time Limiter, LU-SGS Method

Abstract. In the present study, the development of a hybrid, explicit-implicit, second-order TVD (Total Variation Diminishing) method for hyperbolic conservation laws is continued. In our previous works the scheme has been proposed for 1D equations, including the linear advection, Burgers and Euler equations. In the current study, the hybrid scheme is generalized for the 2D Euler equations on unstructured grids. The scheme is of the second order accuracy in space and time for both explicit and implicit modes. In order to make the scheme TVD, space and time TVD limiters are applied, with the latter being generalized for unstructured mesh. The nonlinear system of discretized equations is solved using the Lower-Upper-Symmetric-Gauss-Seidel (LU-SGS) approximate factorization method for unstructured grids. In order to eliminate the factorization and linearization errors, internal iterations are introduced at each time step. Local transient grid adaptation is applied near solution peculiarities, such as shock waves and contact surfaces. The lower and upper matrices in the LU-SGS scheme are formed via reordering of grid nodes at each time step. The new hybrid scheme is applied to a number of test problems chosen to represent the cases with various sources of temporal stiffness. The numerical results demonstrate the ability of the proposed hybrid scheme to produce the same accuracy as the purely explicit scheme while reducing the computational time.

1 INTRODUCTION

Explicit schemes are widely used for simulations of unsteady high-speed flows with shock waves. However, in some shock wave flows the time step of explicit time marching becomes severely restricted by particular conditions in a relatively small flow area while the rest of the computational domain admits much higher time steps. There may be different sources of such *temporal stiffness*, e.g., small geometrical features; locally high temperatures and velocities; regions where viscous effects are essential. In this case one may benefit from a hybrid, explicit-implicit, scheme which would turn into the implicit

mode in the flow regions causing temporal stiffness while the rest of the flow would be simulated in the explicit mode. A number of such schemes were proposed in the past, with, arguably, the most advanced technique being the hybrid scheme by Men'shov and Nakamura [1]. This scheme (M-N) is of the second order in space but only of the first order of accuracy in time in the fully implicit and hybrid modes, and does not belong to the class of TVD (Total Variation Diminishing) schemes. In our previous works [2, 3] we suggested a new hybridization approach and, inspired by the work [4], introduced a new TVD time limiter for our hybrid scheme via the application of Harten's theorem. These resulted in the hybrid scheme for 1D linear/nonlinear scalar conservation laws, which is a TVD one, of the second order accuracy both in space and time in all modes and, as a result, less dissipative than the M-N scheme. Additionally, the hybrid scheme for the 1D Euler equations has been introduced in [5].

The present paper deals exclusively with the generalization of the hybrid scheme for the 2D Euler equations on adaptive unstructured triangular grids with node-centered control volumes. In Section 2, the governing equations are given. Section 3 is devoted to their discretization using the hybrid scheme. The hybridization is achieved by having explicit and implicit portions of the left and right values for the Riemann problem at each cell interface. These values are calculated using the spatial and temporal reconstructions of primitive variables, which are subjected to space and time TVD limiters. The resulting system of non-linear equations is linearized and then solved by the LU-SGS method for unstructured grids. Grid reordering is done at each time step during the solution procedure. Finally, the developed hybrid second-order TVD technique is applied to some 2D demonstrative problems in Section 4 followed by the conclusions (Section 5).

2 GOVERNING EQUATIONS

The Euler equations in conservative form for a control volume Ω bounded by the surface $\partial\Omega$ with the normal vector $\mathbf{n}$ can be written as follows:

$$\frac{\partial}{\partial t}\int_{\Omega}\mathbf{U}\mathrm{d}\Omega + \oint_{\partial\Omega}\mathbf{F}\mathrm{d}S = 0 \ , \tag{1}$$

$$\mathbf{U} = \begin{bmatrix} \rho \\ \rho u \\ \rho v \\ \rho E \end{bmatrix}, \ \mathbf{F} = \begin{bmatrix} \rho V \\ \rho u V + n_x p \\ \rho v V + n_y p \\ (\rho E + p)V \end{bmatrix} \ , \tag{2}$$

with $V = \mathbf{V} \cdot \mathbf{n}$. Here, $\mathbf{V} = (u, v)$ is the velocity vector, ρ – density, p – pressure, E – the specific total energy.

3 NUMERICAL DISCRETIZATION

Discretization of the above equations on an unstructured triangular grid with non-overlapping control volumes around each node (see Fig. 1) results in the following discrete

equations for each node i:

$$\mathbf{U}_i^{n+1} = \mathbf{U}_i^n - \frac{\Delta t}{\Omega_i} \sum_j \mathbf{F}_\sigma^\omega S_\sigma \ , \tag{3}$$

where j are the neighbors of node i; Ω_i is the volume of cell i. Here, σ denotes the values at the control volume face between nodes i and j while S_σ is the absolute value of the respective area vector.
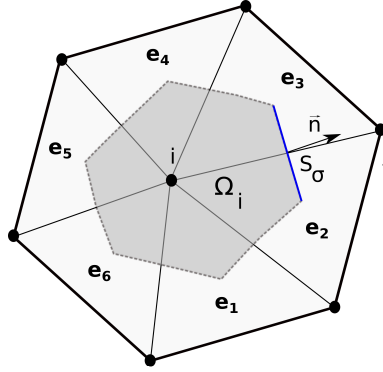

Figure 1: Schematic representation of a control volume.

In Eq. (3) $\mathbf{F}_\sigma^\omega$ is evaluated using the Riemann problem solution at each face with the following left and right values for primitive variables $\mathbf{W} = (\rho, u, v, p)$:

$$\mathbf{W}_L^\omega = \omega_i \left[\tfrac{1}{2}(\mathbf{W}_i^n + \mathbf{W}_i^{n+1/2}) + \tfrac{1}{2}(\overline{\nabla\mathbf{W}})_i^n \cdot \overrightarrow{ij} \right] +$$
$$+ (1 - \omega_i) \left[\mathbf{W}_i^{n+1} + \tfrac{1}{2}(\overline{\nabla\mathbf{W}})_i^{n+1} \cdot \overrightarrow{ij} - \tfrac{1-\omega_i}{2}(\overline{\Delta_t\mathbf{W}})_i^{n+1} \right] \ , \tag{4}$$

$$\mathbf{W}_R^\omega = \omega_j \left[\tfrac{1}{2}(\mathbf{W}_j^n + \mathbf{W}_j^{n+1/2}) - \tfrac{1}{2}(\overline{\nabla\mathbf{W}})_j^n \cdot \overrightarrow{ij} \right] +$$
$$+ (1 - \omega_j) \left[\mathbf{W}_j^{n+1} - \tfrac{1}{2}(\overline{\nabla\mathbf{W}})_j^{n+1} \cdot \overrightarrow{ij} - \tfrac{1-\omega_j}{2}(\overline{\Delta_t\mathbf{W}})_j^{n+1} \right] \ , \tag{5}$$

where ω_i is the hybridization coefficient. It defines the portion of the explicit mode at each grid node ($\omega = 1$ for fully explicit mode and $\omega = 0$ for fully implicit mode). Values of $\mathbf{W}_i^{n+1/2}$ for the explicit portion of the scheme come from the predictor step which employs no Riemann solver and can be written as follows:

$$\mathbf{U}_i^{n+1/2} = \mathbf{U}_i^n - \frac{\Delta t}{\Omega_i} \sum_j \mathbf{F}(\mathbf{W}_\sigma^{\text{in}}) S_\sigma \ , \tag{6}$$

where $\mathbf{W}_\sigma^{\text{in}}$ is the primitive variables at the inner side of the control volume surface:

$$\mathbf{W}_\sigma^{\text{in}} = \mathbf{W}_i^n + \frac{1}{2}(\overline{\nabla\mathbf{W}})_i^n \cdot \overrightarrow{ij} \ . \tag{7}$$

3

3.1 The hybridization coefficient

The hybridization coefficient ω_i could be determined as follows. At first, a part (sub-domain) of the whole computation domain D, *which does not include the source of stiffness*, is identified as D_{exp}. The time step for the hybrid scheme is chosen to be the maximum allowable time step, Δt, in this sub-domain for the fully explicit scheme, which can be obtained from the CFL condition:

$$\Delta t = \min_{i \in D_{\text{exp}}} \hat{\nu} \frac{\Delta L_i}{|\mathbf{V}_i| + c_i}, \tag{8}$$

where $\hat{\nu} < 1$; ΔL_i is the characteristic size of the control volume i, and c_i is the speed of sound. The hybridization coefficient ω_i for each node may be then assigned as:

$$\omega_i = \min\left\{1, \frac{1}{\nu_i}\right\}, \quad \text{where} \quad \nu_i = \frac{(|\mathbf{V}_i| + c_i)\Delta t}{\Delta L_i}. \tag{9}$$

With this choice the scheme is to be in the fully explicit mode in D_{exp} ($\omega_i = 1$ in D_{exp}). It can be shown that this choice satisfies the stability condition of the hybrid scheme.

3.2 Space and time TVD limiters

In order to enhance the spatial and temporal accuracy of the scheme, two types of reconstruction of primitive variables are used in Eqs. (4) and (5). The first one is the limited spatial linear reconstruction within a control volume with the gradient $\overline{\nabla \mathbf{W}}_i$, which could be determined, for example, via the *minmod* limiter based on gradients $(\nabla \mathbf{W})_e$ in the triangles e sharing node i:

$$\left(\overline{\frac{\partial \mathbf{W}}{\partial \alpha}}\right)_i = \underset{e}{\text{minmod}}\left[\left(\frac{\partial \mathbf{W}}{\partial \alpha}\right)_e\right], \quad \alpha = x, y. \tag{10}$$

The second one is the limited time reconstruction in the implicit portion of the left and right face values. Inspired by [4], this time limiter was first introduced for the 1D hybrid scheme in [3, 5] using Harten's theorem. Here, it is generalized for the reconstruction of primitive variables on unstructured grids:

$$(\overline{\Delta_t \mathbf{W}})_i^{n+1,s} = \max\left\{0, \min\left\{\min_j\left[\beta(\mathbf{W}_i^{n+1,s} - \mathbf{W}_i^n) + (\overline{\Delta_t \mathbf{W}})_j^{n+1,s-1}\right], \mathbf{W}_i^{n+1,s} - \mathbf{W}_i^n\right\}\right\}, \tag{11}$$

for non-negative $\mathbf{W}_i^{n+1,s} - \mathbf{W}_i^n$ and

$$(\overline{\Delta_t \mathbf{W}})_i^{n+1,s} = \min\left\{0, \max\left\{\max_j\left[\beta(\mathbf{W}_i^{n+1,s} - \mathbf{W}_i^n) + (\overline{\Delta_t \mathbf{W}})_j^{n+1,s-1}\right], \mathbf{W}_i^{n+1,s} - \mathbf{W}_i^n\right\}\right\}, \tag{12}$$

for negative $\mathbf{W}_i^{n+1,s} - \mathbf{W}_i^n$, where

$$\beta = \frac{2}{\nu_i^s} \cdot \frac{1 - \omega_i^s \nu_i^s (2 - \omega_i^s \nu_i^s)}{(1 - \omega_i^s)^2}. \tag{13}$$

The iterative nature of the time limiter is to be noted: the index s represents the iteration number to be introduced in the next subsection.

3.3 Solution of the discretized equations

As the first step, the system of nonlinear equations (3) with Eqs. (4) and (5) is to be linearized. Newton's linearization of numerical fluxes can be written as follows:

$$\delta\mathbf{U}_i^s + \Delta\mathbf{U}_i^s + \frac{\Delta t}{\Omega_i}\sum_j(\mathbf{F}_\sigma^{\omega,s} + \delta\mathbf{F}_\sigma^{\omega,s})S_\sigma = 0 , \tag{14}$$

where s is the iteration number, $\delta\mathbf{U}_i^s = \mathbf{U}_i^{n+1,s+1} - \mathbf{U}_i^{n+1,s}$ and $\Delta\mathbf{U}_i^s = \mathbf{U}_i^{n+1,s} - \mathbf{U}_i^n$.

Introducing the unsteady residual as $\mathbf{R}_i^{\omega,s} = \Delta\mathbf{U}_i^s + \frac{\Delta t}{\Omega_i}\sum_j\mathbf{F}_\sigma^{\omega,s}S_\sigma$ one arrives at the following form:

$$\delta\mathbf{U}_i^s + \frac{\Delta t}{\Omega_i}\sum_j\delta\mathbf{F}_\sigma^{\omega,s}S_\sigma = -\mathbf{R}_i^{\omega,s} . \tag{15}$$

The subsequent linearization and factorization follows the ideas from [1, 6, 7]. Only the first order fluxes are subjected to linearization and the hybridization coefficient ω is assumed to be frozen at each iteration and treated as a constant. Moreover, for the purpose of linearization the fluxes are approximated by the following function:

$$\mathbf{F}_\sigma = 0.5\big[\mathbf{F}_\sigma(\mathbf{U}_L) + \mathbf{F}_\sigma(\mathbf{U}_R) - (r_A(\mathbf{U}_R)\mathbf{U}_R - r_A(\mathbf{U}_L)\mathbf{U}_L)\big] , \tag{16}$$

where r_A is the spectral radius of the Jacobian $\mathbf{A} = \partial\mathbf{F}/\partial\mathbf{U}$. Consequently, the flux increments can be linearized as:

$$\delta\mathbf{F}_\sigma^{\omega,s} = (1 - \omega_i)\mathbf{A}_\sigma^{(1)}\delta\mathbf{U}_i^s + (1 - \omega_j)\mathbf{A}_\sigma^{(2)}\delta\mathbf{U}_j^s , \tag{17}$$

where

$$\mathbf{A}_\sigma^{(1)} = 0.5[\mathbf{A}_\sigma(\mathbf{U}_i) + r_A(\mathbf{U}_i)\mathbf{I}] \quad \text{and} \quad \mathbf{A}_\sigma^{(2)} = 0.5[\mathbf{A}_\sigma(\mathbf{U}_j) - r_A(\mathbf{U}_j)\mathbf{I}] , \tag{18}$$

and $\mathbf{I}$ is the identity matrix. Using the linearized fluxes, Eq. (15) can be written as:

$$\delta\mathbf{U}_i^s + \frac{\Delta t}{\Omega_i}\sum_j\left[(1 - \omega_i)\mathbf{A}_\sigma^{(1)}\delta\mathbf{U}_i^s + (1 - \omega_j)\mathbf{A}_\sigma^{(2)}\delta\mathbf{U}_j^s\right]S_\sigma = -\mathbf{R}_i^{\omega,s} . \tag{19}$$

After some rearrangements to form upper and lower matrices for subsequent LU (Lower-Upper) factorization it reads as follows:

$$\left[\mathbf{I} + \frac{\Delta t}{\Omega_i}\sum_j(1 - \omega_i)\mathbf{A}_\sigma^{(1)}S_\sigma\right]\delta\mathbf{U}_i^s + \frac{\Delta t}{\Omega_i}\sum_{j<i}(1 - \omega_j)\mathbf{A}_\sigma^{(2)}S_\sigma \cdot \delta\mathbf{U}_j^s+$$
$$+\frac{\Delta t}{\Omega_i}\sum_{j>i}(1 - \omega_j)\mathbf{A}_\sigma^{(2)}S_\sigma \cdot \delta\mathbf{U}_j^s = -\mathbf{R}_i^s . \tag{20}$$

To avoid any matrix inversion and reduce computational costs, the combination of LU approximate factorization and Gauss-Seidel relaxation is applied [6]. The resulting equations are:

$$\left[\mathbf{I} + \frac{\Delta t}{\Omega_i}\sum_j(1 - \omega_i)\mathbf{A}_\sigma^{(1)}S_\sigma\right]\delta\mathbf{U}_i^{s,*} + \frac{\Delta t}{\Omega_i}\sum_{j<i}(1 - \omega_j)\mathbf{A}_\sigma^{(2)}S_\sigma \cdot \delta\mathbf{U}_j^{s,*} = \mathbf{R}_i^s \tag{21}$$

5

$$\left[\mathbf{I} + \tfrac{\Delta t}{\Omega_i}\sum_j(1-\omega_i)\mathbf{A}_\sigma^{(1)}S_\sigma\right]\delta\mathbf{U}_i^s + \tfrac{\Delta t}{\Omega_i}\sum_{j>i}(1-\omega_j)\mathbf{A}_\sigma^{(2)}S_\sigma \cdot \delta\mathbf{U}_j^s =$$
$$= \left[\mathbf{I} + \tfrac{\Delta t}{\Omega_i}\sum_j(1-\omega_i)\mathbf{A}_\sigma^{(1)}S_\sigma\right]\delta\mathbf{U}_i^{s,*} . \tag{22}$$

It is known that for any closed surface $\partial\Omega$ the following identity holds ([7]):

$$\int_{\partial\Omega}\mathbf{A}_\sigma \mathrm{d}S_\sigma = 0 . \tag{23}$$

Therefore we have:

$$\frac{\Delta t}{\Omega_i}\sum_j(1-\omega_i)\mathbf{A}_\sigma^{(1)}S_\sigma = \frac{1}{2}\frac{\Delta t}{\Omega_i}\sum_j(1-\omega_i)r_A(\mathbf{U}_i)S_\sigma . \tag{24}$$

Substitution of Eq. (18) into Eqs. (21) and (22) and application of the above Eq. (24) results in the two-step, forward and backward, procedure for finding $\delta\mathbf{U}_i^s$ at current iteration without any matrix inversions:

$$\delta\mathbf{U}_i^{s,*} = -\frac{1}{1+\frac{1}{2}\frac{\Delta t}{\Omega_i}\sum_j(1-\omega_i)r_A(\mathbf{U}_i^s)S_\sigma}\left[\mathbf{R}_i^s + \frac{1}{2}\frac{\Delta t}{\Omega_i}\sum_{j<i}(1-\omega_j)[\mathbf{A}_\sigma(\mathbf{U}_j^s)-r_A(\mathbf{U}_j^s)\mathbf{I}]S_\sigma\cdot\delta\mathbf{U}_i^{s,*}\right]$$
$$\tag{25}$$
$$\delta\mathbf{U}_i^s = \delta\mathbf{U}_i^{s,*} - \frac{1}{1+\frac{1}{2}\frac{\Delta t}{\Omega_i}\sum_j(1-\omega_i)r_A(\mathbf{U}_i^s)S_\sigma}\times\frac{1}{2}\frac{\Delta t}{\Omega_i}\sum_{j>i}(1-\omega_j)[\mathbf{A}_\sigma(\mathbf{U}_j^s)-r_A(\mathbf{U}_j^s)\mathbf{I}]S_\sigma\cdot\delta\mathbf{U}_i^s .$$
$$\tag{26}$$

Index s denotes the known values from the previous iteration. The values at iteration $s+1$ are then found from $\mathbf{U}_i^{n+1,s+1} = \mathbf{U}_i^{n+1,s} + \delta\mathbf{U}_i^s$.

3.4 Grid adaptation

Local grid adaptation in the form of the classical h-refinement [8] is performed near localized flow field features (shock and expansion wave fronts, contact discontinuities, vortices etc.) as dictated by the refinement/coarsening sensor based on second order differences of density [9]:

$$E_i = \max_e\left(\frac{|(\nabla\rho)_e - \overline{(\nabla\rho)}_i|}{|(\nabla\rho)_e| + |\overline{(\nabla\rho)}_i| + \epsilon|\rho_i|(\Delta L_i)^{-1}}\right) , \tag{27}$$

where, as above, index e denotes triangles sharing node i and ΔL_i is the characteristic size of the control volume i. The quantity ϵ represents a noise filter coefficient; $\overline{(\nabla\rho)}_i$ is the weighted average gradient of density in the control volume i based on gradients in the triangles sharing node i. Refinement and coarsening in the vicinity of each node are governed by the corresponding values of E_i and the prescribed refinement and coarsening thresholds T_r and T_c. If $E_i > T_r$ the node i is marked for refinement of neighbouring triangles while if $E_i < T_c$ the node may be removed.

3.5 Unstructured grid reordering

As mentioned before, the LU-SGS scheme is used for time integration, which is matrix inversion free and storage-efficient. The definition of the lower and upper matrices for unstructured grids is not straightforward, and it may affect the convergence rate of iterations. In the above sections, similarly to [6], forward and backward sweeps are designated to be in accordance with grid node numbers. However, since nodes of unstructured grids are, generally, numbered in a random order, node-number-based sweeps may lead to low iteration convergence rates or even the lack of thereof. Therefore, a grid reordering method is implemented, similarly to what has been proposed in [10], which groups nodes into *hyperplanes* and the forward and backward sweeps are then performed based on the hyperplane numbers rather than node numbers. This partitioning is done in such a way that nodes from the same hyperplane are not connected to each other. In other words, all neighbors of a node are marked with hyperplane numbers different from the one for that specific node.

4 RESULTS

In this section, the new hybrid scheme is applied to two test problems chosen to represent some sources of stiffness mentioned in Section 1.

4.1 Blast wave propagation

The first test problem is the simulation of a cylindrical blast wave induced by instantaneous energy deposition within a small cylindrical region. The temporal stiffness is due to the high temperature (and hence, the high speed of sound) core remaining at the explosion center after the blast wave has been formed and moved away from the center. The initial state inside the cylindrical energy deposition region of radius 1 corresponds to a gas at rest with a high pressure $p_1 = 10^6$ and a high density $\rho_1 = 100$. The gas can be interpreted as the one originating from denotation of an explosive charge, and, hence, it is to be called below "detonation gas". The ambient initial conditions are a quiescent gas with a low pressure $p_0 = 10^{-3}$ and a low density $\rho_0 = 1$. All the initial values are non-dimensional. Both the ambient gas and the detonation gas are considered to be ideal with the constant specific heat ratio $\gamma = 1.4$. The choice of initial parameters is made to allow for the comparison of numerical solutions with the Sedov-Taylor analytical solution for the cylindrical strong point explosion problem (for the purpose of code validation).

In order to reduce the simulation time, only a sector is modeled with 2391 initial grid nodes. Three levels of refinement are applied, and the computation proceeds till $t = 300$, when the blast wave is close to the outer cylindrical boundary. Instant pressure, temperature, and hybridization coefficient distributions are shown in Fig. 2a-c. Near the explosion center the contours of temperature and hybridization coefficient are not cylindrical due to relatively coarse mesh at the initial high/low pressure interface of small radius, which induces grid-related disturbances growing in the course of flow development.

(a) Pressure contours

(b) Temperature contours (log scale)

(c) Hybridization coefficient ω
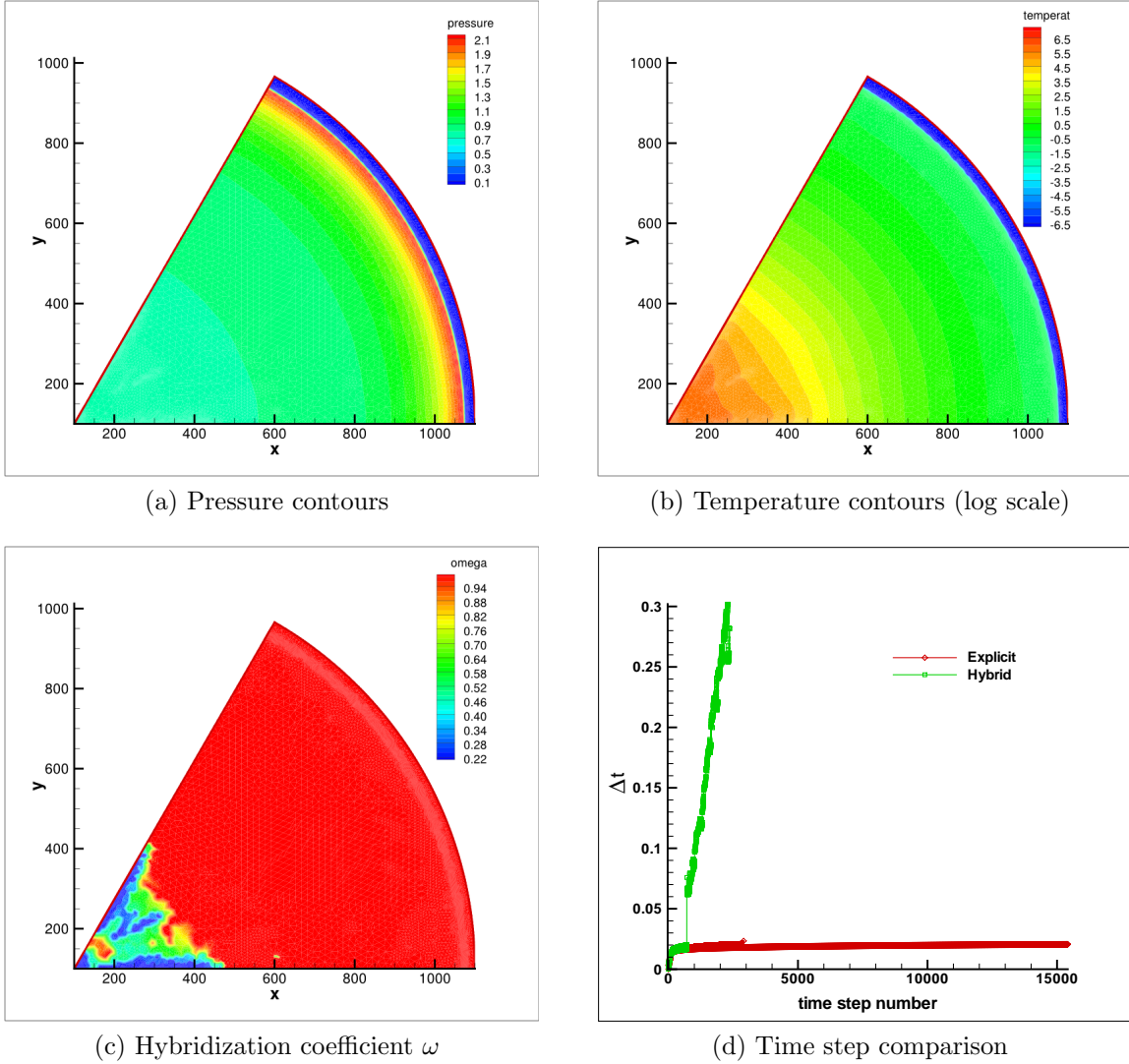
(d) Time step comparison

Figure 2: Cylindrical blast wave propagation problem: (a)-(c) Instant pressure, temperature, and hybridization coefficient distributions for a time moment when the blast wave is approaching the outer boundary of the computational domain; (d) Time step history for the hybrid and fully explicit schemes.

As seen in Fig. 2b,d, the high-temperature core near the explosion center at (100,100) would cause very small time steps as compared to the rest of the domain for a fixed Courant number. In view of that, the sub-domain $D_{\exp}$ is defined to correspond to the ambient gas, so that not to include the high-temperature core. To track the detonation/ambient gas boundary, a mixture of two gases, the detonation and ambient ones, is considered (even though physically these gases are the same in the present test computa-
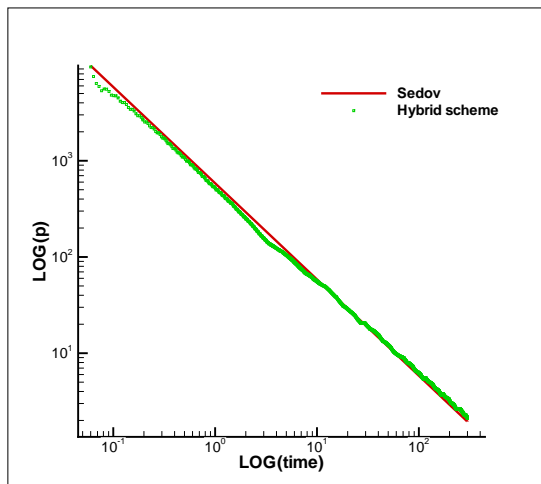
8

Figure 3: Cylindrical blast wave propagation problem: comparison of the pressure history behind the cylindrical shock front for the new hybrid explicit-implicit method with the analytical solution by Sedov [11].

tions), and one additional advection equation for the mass fraction of the detonation gas is included into the governing equations.

The explicit sub-domain D_{exp} consists of grid nodes where the mass fraction of the detonation gas is lower than a certain threshold. This sub-domain includes the blast wave and represents most of the computational domain. The time step value is based on the solution within the explicit sub-domain D_{exp} and $\hat{\nu} = 0.5$, see Eq. (8). Since the source of stiffness (the high-temperature/high speed of sound region) is outside of this sub-domain, the resulting time step is larger than the one which would be obtained from the CFL condition applied to the whole computational domain (which must be done if the fully explicit mode is to be used).

In the explicit sub-domain the scheme is then in its explicit mode (see $\omega \sim 1$ region in Fig. 2c). On the other hand, it is predominantly in the implicit mode closer to the explosion center where the Courant numbers are higher due to high temperatures. This results in almost 5 times shorter CPU time as compared to the same simulation done with the fully explicit method and $\hat{\nu} = 0.5$ in the whole domain.

Comparison between the time step values of the hybrid and fully explicit methods at each time step is presented in Fig. 2d. Both simulations are done till the same final time moment mentioned above. It is seen that the time steps of the explicit method are much smaller than those of the hybrid one; thus, the explicit scheme needs more time steps to reach the same time moment, which leads to higher CPU time.

To compare the results of the hybrid scheme and the analytical solution for the cylindrical strong point explosion [11], the history of pressure values behind the blast wave front is depicted in logarithmic scale in Fig. 3. It is seen that the results of the hybrid scheme match the analytical solution very well.

9

4.2 Shock wave diffraction

The second test problem is the shock wave diffraction over a 90° corner. Shock wave diffraction at a sharp edge is of frequent occurrence in compressible shocked flows. Furthermore, this problem has been widely used for validation of numerical schemes. In this problem the potential source of stiffness is related to large magnitudes of velocity downstream from the sharp corner, which may reduce the time step values of explicit schemes. The effect of high velocities in the expansion fan is partially compensated by the decrease in temperature (and, hence, the speed of sound) but it may still be essential. Furthermore, it is to be noted that some shock-capturing schemes based on the mass, momentum and total energy conservation laws produce abnormally high velocities in the immediate vicinity of the corner (a few cells downstream of it along and near the wall), where the centered expansion fan cannot be resolved regardless of grid cell size.

In the present computations the incident shock Mach number is chosen to be 10 in order to induce larger velocities around the corner and make their effect pronounced as much as possible. The initial shock location is at $x = -10$ while the corner is located at $(0,0)$. In front of the shock, the gas is at rest with the non-dimensional pressure and density equal to unity ($\rho_0 = 1$ and $p_0 = 1$). The specific heat ratio is $\gamma = 1.4$. The background grid contains 6385 nodes. Three levels of grid refinement are used.

Shock diffraction over a corner leads to the formation of the contact surface separating the gas which has passed through the diffracted shock and the one which flows around the corner. This contact surface can conveniently serve as the boundary of the explicit subdomain D_{exp}, which would not then include the region with high velocities downstream from the corner. To track the contact surface, similar to the previous test problem, the approach with a two-species mixture (with both species being the same gas) and one additional advection equation is used.

The computation is carried out till $t = 10$. Instant pressure, velocity and hybridization coefficient contours of the flow field at that time moment are presented in Fig. 4. It is seen that similar to the previous test problem, most of the domain is computed in the explicit mode ($\omega = 1$) based on the Courant number $\hat{\nu} = 0.7$, except the area near the corner where a high velocity region exists. As already mentioned above, within the most part of the centered expansion fan high velocities (see Fig. 4b) are compensated by the decrease in temperature and hence do not lead to significant decrease of the local time step, and, hence, the hybridization coefficient, throughout the whole expansion fan (see Fig. 4c). However, according to Fig. 4c, there is a small region in the immediate vicinity of the corner where the hybridization coefficient is significantly less than 1. This region is calculated with the implicit mode of the scheme with Courant numbers higher than 1.

As a result, time steps of the hybrid scheme are larger than those for the explicit method (see Fig. 4d where time step values are shown), which makes the simulation faster. In this case, the CPU time of the hybrid scheme is almost two times shorter than that for the fully explicit scheme with $\hat{\nu} = 0.7$ in the whole domain.
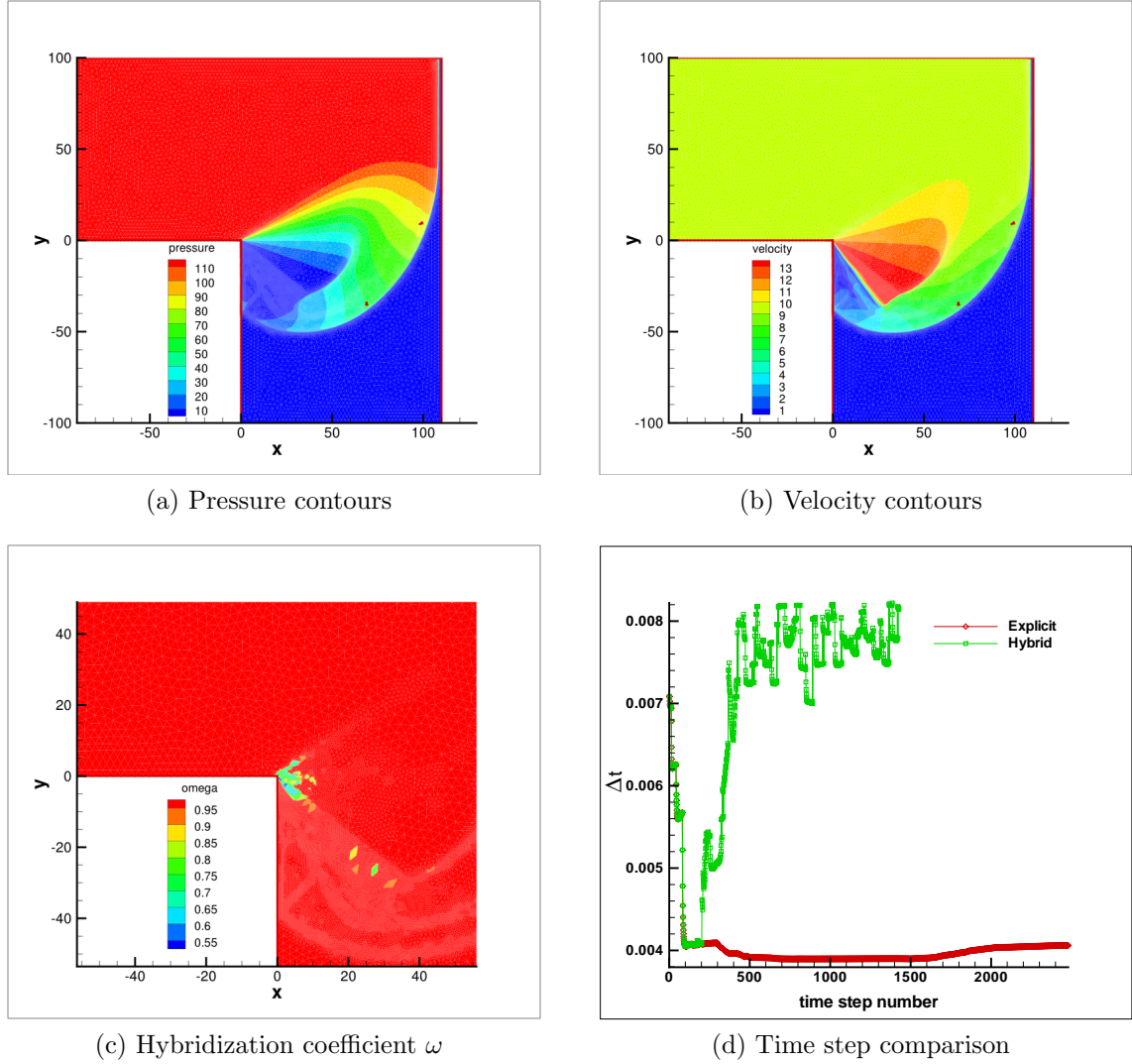
(a) Pressure contours

(b) Velocity contours

(c) Hybridization coefficient ω

(d) Time step comparison

Figure 4: Shock wave diffraction over a 90° corner: (a)-(c) Instant pressure, velocity, and hybridization coefficient distributions; (d) Time step history for the hybrid and fully explicit schemes.

5 CONCLUSIONS

The results show the ability of the proposed hybrid scheme to handle problems with temporal stiffness. In all problems, the proposed hybrid scheme results in the solutions of the same accuracy as the ones produced by its fully explicit mode (the MUSCL-Hancock scheme) while the computational time is reduced. Due to calculations with higher Courant numbers in some regions of the computational domain, hybrid scheme computations are faster than simulations of the same problem with the fully explicit scheme.

REFERENCES

[1] Men'shov, I. and Nakamura, Y. Hybrid explicit-implicit, unconditionally stable scheme for unsteady compressible flows. *AIAA J.* (2004) **42**(3):551–559.

[2] Norouzi, F. and Timofeev, E. A hybrid, explicit-implicit, second order in space and time TVD scheme for one-dimensional scalar conservation laws. *AIAA Paper* 2011-3046, 9p.

[3] Norouzi, F. and Timofeev, E. A Hybrid explicit-implicit second order TVD scheme: The scalar nonlinear equations case. *Proc. of 19th Annual Conference of CFD society of Canada*, Montreal, QC, April 2011, Paper CFDSC2011-1A4, 6 p.

[4] Duraisamy, K. and Baeder, J. Implicit scheme for hyperbolic conservation laws using nonoscillatory reconstruction in space and time. *SIAM J. on Scientific Computing* (2007) **29**(6):2607–2620.

[5] Timofeev, E. and Norouzi, F. Application of a new hybrid explicit-implicit flow solver to 1D unsteady flows with shock waves. In: K. Kontis (Ed.), *Proc. of the 28th International Symposium on Shock Waves*, Manchester, UK, July 2011, Springer, vol. **2**, pp. 245–250, 2012.

[6] Men'shov, I. and Nakamura, Y. On implicit Godunov's method with exactly linearized numerical flux. *Computers and Fluids* (2000) **9**:595–616.

[7] Men'shov, I. and Nakamura, Y. Implementation of the LU-SGS method for an arbitrary finite volume discretization. *Proceedings of the 9th Japanese Conference on CFD*, Tokyo, p. 123, 1995.

[8] R. Löhner. An adaptive finite element scheme for transient problems in CFD. *Comp. Meth. Appl. Mech. Eng.* (1987) **61**:323-338.

[9] Saito, T., Voinovich, P., Timofeev, E., and Takayama, K. Development and application of high-resolution adaptive numerical techniques in Shock Wave Research Center. In:*"Godunov Methods: Theory and Applications"*, Edited Review, E.F. Toro (Ed.), Kluwer Academic/Plenum Publishers, New York, USA, 2001, pp. 763–784.

[10] Sharov, D. and Nakahashi, K. Reordering of hybrid unstructured grids for lower-upper symmetric Gauss-Seidel computations. *AIAA J.* (1998) **36**(3):484–486.

[11] Sedov, L.I. *Similarity and dimensional methods in mechanics.* Academic Press, New York, NY, (1959).